

SOAR-OSIRIS observations of the Sh 2-307 HII region: Triggered star formation beyond the solar circle

A. Roman-Lopes^{1*}

¹*Physics Department - Universidad de La Serena - Cisternas, 1200 - La Serena - Chile*

ABSTRACT

This work aims to the study of the Sh 2-307 HII region and related stellar population. Near-infrared imaging and spectroscopic observations in the direction of Sh 2-307 were performed using OSIRIS at SOAR Telescope. The photometric data were analysed from color-color, and colour-magnitude diagrams, while the spectroscopic results were interpreted from the comparison of the science spectra with that obtained from known OB stars. From J-, H- and K-band spectra of the brightest source in the cluster, we conclude that it has a near-infrared spectra compatible with that taken for O9v-O9.5v stars. Using the derived spectral type and the respective J, H and K-band photometry, we compute a heliocentric distance of 3.2 ± 0.5 kpc, which for $R_0 = 8$ kpc, puts this cluster at more than 10 kpc from the Galactic centre. From the $\text{Br}\gamma$, H_2 , and continuum narrow-band images we were able to detect both the NIR counterpart of the associated HII region, as well as, the interface between the ionised and the cool molecular gas. Using the 5 GHz continuum flux density taken from the PMN catalogue and the $\text{Br}\gamma$ narrow band image we estimate that the HII region has a mean diameter of 0.94 ± 0.15 pc, mean electron density of 550 cm^{-3} and an estimated dynamical age of 1.6×10^6 years. The large fraction of sources presenting excess emission at $2\mu\text{m}$ suggests that the stellar population is very young, with many sources still in the pre-main sequence accreting phase. By the use of theoretical pre-main sequence tracks we derived a cluster mean age of about 2.5 Myears, and from the analyses of the fraction of excess emission sources as a function of their spatial distribution we found evidence for an age spread for the embedded pre-main sequence stellar population. Finally, from the study of the spatial distribution of the low-mass sources relative to the main-cluster source and associated photo-dissociation zones, we conclude that the O-type star probably has been triggering the star formation process in the region.

Key words: (ISM:) H II regions; Infrared: stars; Stars: pre-main sequence; Galaxy: structure

1 INTRODUCTION

The studies of Galactic stellar clusters are important to improve our knowledge of the physical processes leading to their formation and evolution. The stars in a cluster share the same parental molecular cloud, are formed more or less simultaneously in time, and contain samples of stars that span a wide range of stellar masses within a relatively small volume of space. In this sense, they can be used to provide tests for the stellar evolution theory. As an example, we notice that such systems are the smallest physical entities in which one can perform a meaningful determination of the stellar initial mass function (IMF) (Salpeter, 1955; Scalo, 1986). On the other hand, because young stellar clusters are excellent tracers of the spiral pattern of external galaxies,

the study of the spatial distribution of the Galactic clusters play a key role in the understand of the structure and evolution of our own galaxy.

Sharpless 307 (Sh 2-307), is a small HII region located in the outer Galaxy at $l = 234.58$, $b = +0.84$ (Sharpless, 1959). It was detected by the Parkes-MIT-NRAO (PMN) 4.85GHz Survey as a radio source measuring about $1.3' \times 1.2'$, with integrated flux density $S_{5\text{GHz}}$ of 726 ± 39 mJy. It is part of a complex that was studied by Russeil et al. (1995), who from Fabry-Perot $\text{H}\alpha$ interferometric observations, concluded that the HII regions can be separate in two velocity groups. The first group with $V_{LSR} \sim 16 \text{ km s}^{-1}$, is located at a kinematic distance of 2.2 kpc while the other with $V_{LSR} \sim 43 \text{ km s}^{-1}$, corresponds to a kinematic distance of 4.2 kpc. From this scheme, the Sh 2-307 HII region (with a radial velocity of 37 km s^{-1}) would belongs to the second molecular cloud. However, its radial velocity is somewhat

* roman@dfuls.cl

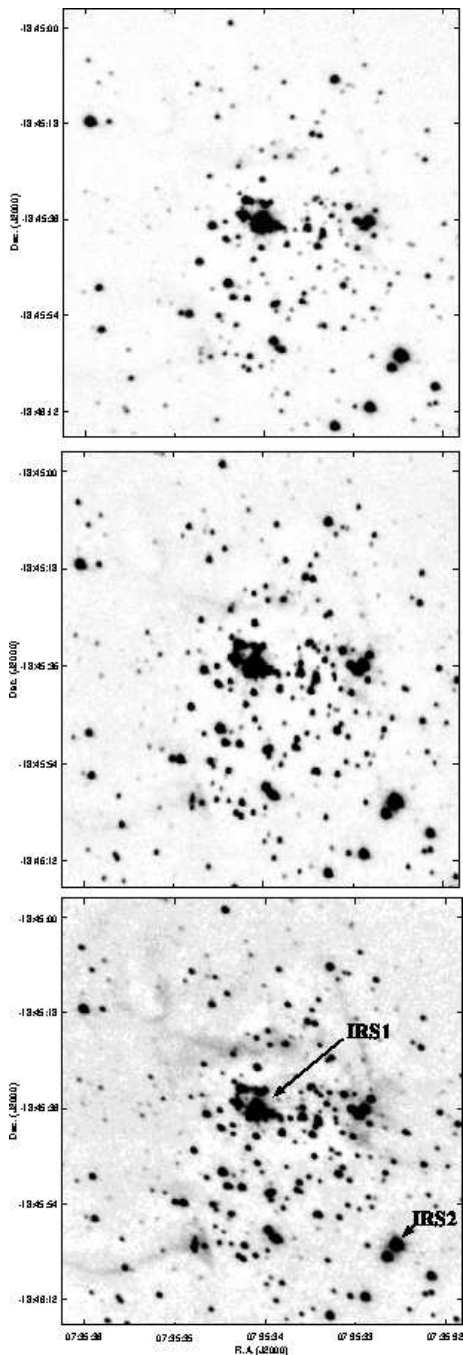


Figure 1. The near-infrared J (top), H (centre) and K_S (bottom) OSIRIS ($70'' \times 60''$) images of the region in the direction of the Sh 2-307 HII region. North is to the top, east to the left.

lower than that for the other HII regions, and as suggested by the authors, a possible explanation for the discrepancy between the velocities of the ionised and molecular material, would come from the effects of a “Champagne flow” (Tenorio-Tagle, 1979), which would be produced by the ionization front of the associated HII region located at the near edge of the molecular cloud. The presence of a far-IR source (IRAS07333-1838) that has colours characteristic of ultra-compact HII regions (Wood & Churchwell, 1989), and the detection of a 22 GHz H_2O maser by Han et al. (1998), suggest that star formation is still occurring there.

Moffat et al. (1979) were the first group to obtain some photometric measurements of point sources in the region. They performed UBV photometry of five objects in the direction of the complex that contains the Sh 2-307 HII region. However, the only point source directly related with this HII region is their source #3 (which has $V = 12.47$, $B - V = 0.79$, $U - B = -0.32$). The other point sources are placed outside the core of the Sh 2-307 HII region, not belonging to the same star forming complex. Hunter & Massey (1990) performed optical spectra for a bright optical source in the core of the Sh 2-307 region, concluding that it might be a B0V star. Dutra et al. (2003), from the analyses of the superficial density of sources in the 2MASS image survey, suggested the presence of a cluster of stars in the direction of Sh 2-307 (identified in their catalogue as cluster candidate #7). Unfortunately, the poor spatial resolution of the 2MASS images do not able one to properly resolve the stars in the inner part of the system.

In this paper we report the results of a near-infrared spectrophotometric survey made in the direction of the core of the Sh 2-307 HII region. For the first time we were able to fully access its stellar content, identifying the main-ionizing source of the cluster and addressing its stellar population. In section 2 we describe the observations and the data reduction procedures, in section 3 we present the results, in section 4 the analyses and discussion, and in section 5 we present our conclusions.

2 OBSERVATIONS AND DATA REDUCTION

In this work we used the Ohio State Infrared Imager/Spectrometer (OSIRIS¹), coupled to the 4.1 m telescope of the Southern Observatory for Astrophysical Research (SOAR). The observatory is placed at Cerro Pachon, Chilean Andes (about 2800 m above the sea level). It was constructed by the consortium of the Brazilian Ministry of Science, the National Optical Astronomy Observatories, the University of North Carolina and Michigan State University.

2.1 OSIRIS imaging observations

High resolution near-infrared (NIR) imaging observations were performed in the direction of Sh 2-307 ($\alpha = 7h35m34.19s$ and $\delta = -18d45m35.6s$, Equ J2000). The data were taken during the 2007 November, 8 night, using the OSIRIS’s f/7 camera, which at the SOAR Telescope produces images with a plate scale of about $0.14''$ per pixel. We used the J , H and K_S broad-band filters and the H_2 , Continuum (at $2.14\mu m$) and $Br\gamma$ narrow-band filters.

From the OSIRIS acquisition images of the region, we

¹ OSIRIS is a collaborative project between the Ohio State University and Cerro Tololo Inter-American Observatory (CTIO) and was developed through NSF grants AST 90-16112 and AST 92-18449. CTIO is part of the National Optical Astronomy Observatory (NOAO), based in La Serena, Chile. NOAO is operated by the Association of Universities for Research in Astronomy (AURA), Inc. under cooperative agreement with the National Science Foundation.

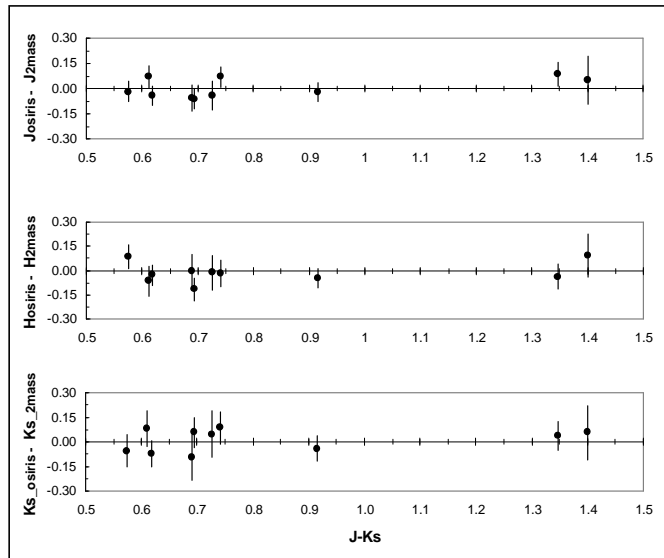


Figure 2. The difference between the OSIRIS and 2MASS J-, H- and K_s -band photometry as function of the $J - K_s$ colours. We can see that there is no need to apply colour correction terms.

detected the presence of extended emission. In order to perform a good subtraction of the thermal background component from the science frames, it is necessary to construct a "clean" median combined image, free of any residual of point sources, as well as, of extended sources. The FOV of the OSIRIS camera in the f/7 mode is about $80''$, which is only a bit larger than the apparent angular size of the cluster, which was estimated as $1'$ by Dutra et al. (2003). This feature could limit our capability to construct useful "sky" frames when using only the science ones. We avoid this problem by performing "on source", and "sky" sequential observations (source-sky-source-sky...). The "sky" frames were taken in a region located about $2'$ east from the cluster centre, with coordinates $\alpha = 7\text{h}35\text{m}42.46\text{s}$ and $\delta = -18\text{d}45\text{m}41.7\text{s}$ (J2000)

Despite the extra amount of time necessary to perform "on-source" and "sky" alternate observations, there are some advantages when using this procedure. From the "sky" frames, we constructed J , H and K_s images that enabled us to perform photometric calibration of the OSIRIS data, using the results from the 2MASS point source catalogue. On the other hand, under the assumption that the point sources in the "sky" region are representative of the "local" Galactic field stellar population, the analyses of their magnitudes and colours, provide additional clues that can help us to identify and exclude the sources that probably do not belong to the star forming region.

We obtained a set of five images per filter for both, the sky and cluster coordinates. This was done following a cross pattern in which the telescope was nodded by $8''$ in the NSEW directions (always from the associated central coordinates). The individual exposure times for the broad- and narrow-band frames were 60s, and in order to guaranty good photometry also for the brightest sources (avoiding saturation), we also took a set of J-, H- and K_s -band short exposure time (5s) images. In order to correct the raw frames by the differences in the pixel response, a set of on-off flat-

field images were taken for each broad- and narrow-band filter we used.

The raw frames were reduced using the CTIO infrared reduction (CIRRED²) package within IRAF³, following the NIR reduction procedures described in Roman-Lopes et al. (2003). The final broad- and narrow-band NIR images for the cluster and "sky" (hereafter named "control") regions, were constructed by shifting and combining the reduced raw frames. The mean values of the full width at half maximum (FWHM) of the point sources in the J-, H- and K_s - band combined images are $0.75''$, $0.70''$ and $0.64''$, respectively.

2.2 NIR spectroscopic observations

The NIR spectroscopic observations of the two brightest sources in the cluster region were made during the 2007 November, 24 night. The J-, H- and K-band spectra were taken using OSIRIS in the Low-Resolution ($R \sim 1200$) multi-order cross-dispersed (XD) mode. In the XD mode, the instrument operates using the f/2.8 camera and the short slit ($27'' \times 1''$), covering the three bands simultaneously in adjacent orders. The spectra were acquired using the standard AB nodding technique (with an offset of $12''$). Individual exposure times at each nod position was 120 s. For each source, we obtained 16 individual frames that resulted in a total individual exposure time of 32 minutes. In order to remove telluric atmospheric absorption effects from the science spectra, nearby A and G spectroscopic standard stars were observed at similar airmasses, before and after the science targets.

The spectroscopic data were reduced using the

² http://www.ctio.noao.edu/instruments/ir_instruments/datared.html

³ IRAF is distributed by the National Optical Astronomy Observatories, which are operated by the Association of Universities for Research in Astronomy, INC, under cooperative agreement with the National Science Foundation

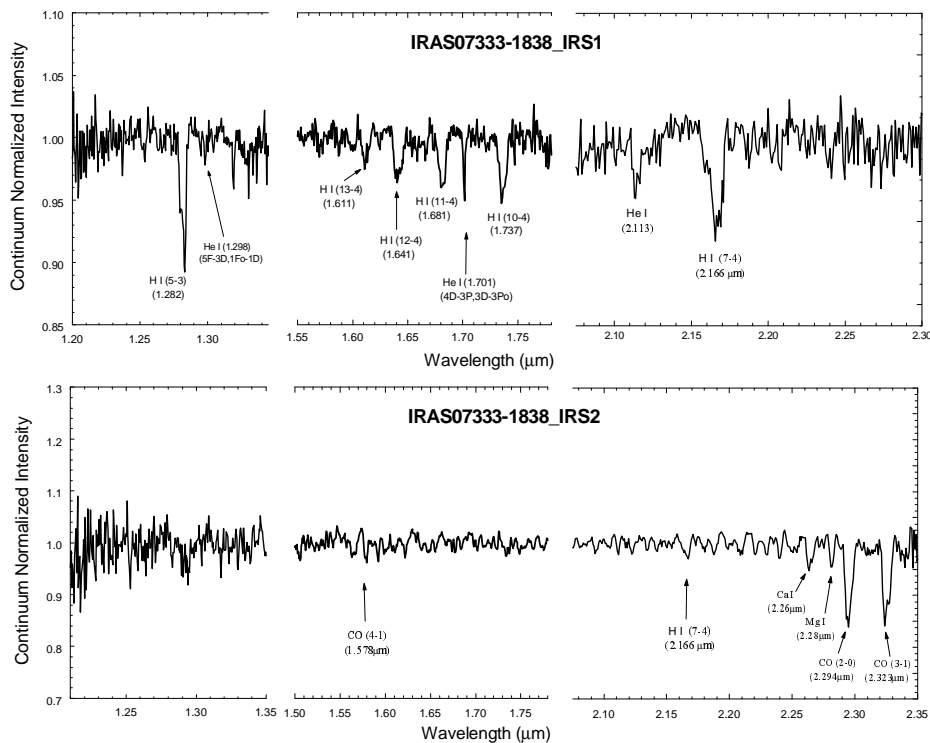


Figure 3. The NIR spectra for the IRS1 and IRS2 sources. The spectral resolution in the *K* band is $R \sim 1200$ and the 1σ uncertainty in the wavelength calibration is about 7 \AA . The mean signal to noise ratio is 120 for IRS1 spectra and about 50 for IRS2 one. The spectra of IRS1 source shows the Hydrogen and Helium recombination lines typical of hot stars, while that for IRS2, presents CO and metallic lines commonly found in late-type stars and young stellar objects.

CIRRED package within IRAF. The two-dimensional frames were sky-subtracted for each pair of images taken at the two nod positions A and B, followed by division of the resultant image by a master flat. Thereafter, wavelength calibration was applied using the sky lines; the typical error (1σ) for this calibration was $\sim 7 \text{ \AA}$. The multiple exposures were combined, followed by one-dimensional extraction of the spectra. Telluric atmospheric correction using the spectroscopic standard stars completed the reduction process. In this last step, we divided the target spectra by the spectrum of the A0v spectroscopic standard star, already free of photospheric features. In this particular case, the Hydrogen series are the main features present in the *J*, *H*- and *K*-bands. The *J* and *K* band hydrogen lines in the spectra of the A0v spectroscopic standard star, were carefully removed by interpolation across their wings, using the continuum points on either side of the line.

In the case of the H-band, the subtraction of the hydrogen absorption lines can not be successfully made directly from the spectrum of the A0v telluric star. The relative position of the multiple lines of the Bracket series and the presence of some strong telluric features, do not permit a good fitting of the adjacent continuum, which is fundamental to remove the line profiles. In order to assure good results, we removed the Hydrogen lines from the A0v H-band spectrum using the procedure applied by Blum et al (1997). The method consists in to obtain a good fitting of the hydrogen lines, using the spectrum obtained by the division of the A

standard star spectrum, by that of the G star. In the case of the G star spectrum, its own H I intrinsic lines (which in general are weaker than that found in the A0v spectra), were previously removed by hand using as template, the NOAO solar atlas of Livingston & Wallace (1991). The last step was to corrected the A0v spectrum by that of the model, obtaining a H-band spectrum free of the hydrogen Bracket lines.

Finally, in order to assure good cancellation of the telluric bands, the task *telluric* of IRAF was employed. The algorithm interactively minimises the RMS in specific sample regions, by adjusting the shifts and scales between the standard and science spectrum to best divide out telluric features present in the latter. The shifting allows for possible small errors in the dispersion zero-points. The intensity scaling allows for differences in the airmass and variations in the abundance of the telluric species. Typical values of the shifts were equivalent to a few tenth of a pixel (about $\sim 2 \text{ \AA}$), while the scaling factors were not larger than 10%.

2.3 The NIR spectra of known OB stars

In order to estimate the spectral type of the brightest source in the cluster, its spectra were compared with that obtained from the known OB stars (hereafter named *templates*), which are present in Table 1. The *J*, *H* and *K* band spectroscopic observations of the template stars were performed in different nights, in which all the spectra were acquired from

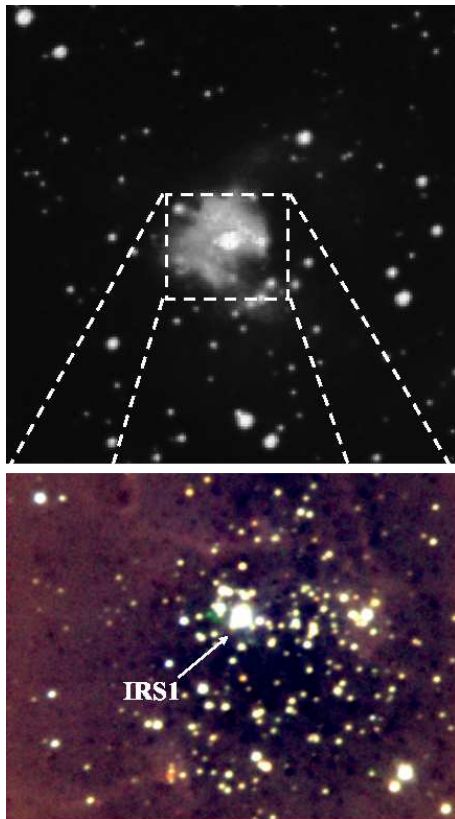


Figure 4. The DSS R-band image (about 5 arcmin in size) of the core of the SH 2-307 HII region (top), and the J- (blue), H- (green) and K_S -band (red) three colour composite image ($\sim 70'' \times 50''$) of the section delineated by the white dotted square in the R-band image. The IRS1 source for which a NIR spectra were taken, is indicated. Note the large quantity of sources around the main source. A cavity inside the cloud (delineated by the K-band emission) is clearly seen. In this figure, North is to the top and east is to the left.

the same equipment used during the observations of the Sh 2-307 sources (e.g. same telescope, instrument setup, and technique described in Section 2.2). It means that all spectra have virtually the same spectral resolution (that can change a bit due to differences in the seeing conditions, airmass, focus, etc), and cover the same spectral range. Due to the brightness of the template stars (all sources have K magnitudes less than 8), the signal-to-noise ratio of the resulting spectra are 150 in excess.

3 RESULTS

3.1 NIR photometry

The J-, H- and K_S -band images of the core of the Sh 2-307 HII region (hereafter named *cluster* region) are shown in Figure 1. The NIR photometry of the point sources in the cluster and control regions were performed using the DAOPHOT (Stetson, 1987) package within IRAF. The selection of the point sources in the NIR images, was made using the task daofind, assuming a detection threshold of 10σ above the local sky. Due to source confusion in some crowded parts of the cluster region, we choose to perform point spread

function (PSF) photometry. The procedure we applied was that described in Roman-Lopes & Abraham (2004), using a PSF radii of 14 pixels for the J- and H- bands and 12 pixels for the K_S -band.

The zero-points for the J-, H- and K_S -band OSIRIS photometry were determined using the results from the 2MASS⁴ all sky point source catalogue (PSC). For each broad band filter, a set of isolate stars in the control images was used to calibrate the OSIRIS photometric data. Only stars with good 2MASS photometry (flags A and B) were used. The mean values of the errors in the zero point magnitudes are 0.03, 0.05 and 0.06 mag for the J-, H- and K_S -bands, respectively. The final photometric errors were calculated as the quadratic sum of the mean zero-point errors mentioned above and the associated photometric uncertainty for each source, as given by the ALLSTAR routine. The values of the completeness limits for J-, H-, and K_S -bands are 17.6, 17.2, and 16.7 mag, respectively, and were derived from the point at which the number of detected sources of magnitude m , $N(m)$ deviates from a straight line in the $\log(N)$ versus m diagram (Roman-Lopes et al. 2003).

We found a good correlation between the OSIRIS photometry and that from the 2MASS survey. The plots with the differences between the OSIRIS and 2MASS J-, H- and K_S -band magnitudes as function of the $J - K_s$ colours are shown in Figure 2. We can see that there is no need to apply colour-term correction in the derived OSIRIS magnitudes. The J-, H- and K_S -band photometry obtained for all sources detected in the cluster region are shown in Table 2 (which is available in its entire form in the electronic version of the article).

3.2 NIR spectra of IRS1 and IRS2 sources

Figure 3 shows the J , H and K band spectra taken for IRS1 and IRS2, the two brightest sources in the cluster region (see Figure 1). The spectra of the IRS1 source present features typical of hot stars. In fact, there are several Hydrogen recombination lines from the Brackett series at $1.611\mu\text{m}$, $1.641\mu\text{m}$, $1.681\mu\text{m}$, $1.737\mu\text{m}$ and $2.166\mu\text{m}$, and also the H α (5-3) Paschen line (at $1.282\mu\text{m}$), the last one in the J band. We also found the HeI lines at $1.701\mu\text{m}$ and $2.113\mu\text{m}$, which indicate that IRS1 must be hotter than a B2V star (Hanson et al. 1996).

The NIR spectra of the IRS2 source is completely different from that taken for IRS1. There are no hydrogen or HeI lines in the H band, and we found only a weak Br γ absorption line in the K band. On the other hand, we can see the CO lines at $1.578\mu\text{m}$, $2.294\mu\text{m}$ and $2.323\mu\text{m}$, which are commonly seen in late-type stars (Ali et al. 1995; Ivanov et al. 2004), as well as, also found in the NIR spectra of young stellar objects (Casali & Matthews 1992, Hoffmeister et al. 2006). In summary, the K-band spectrum of IRS2 is not characteristic of hot stars, but considering its apparent location in the densest part of the cloud and its spatial correlation with some extended emission seen in the R-band image, we can not discard its condition as a member of the cluster, being a candidate to intermediate mass young stellar object (YSO).

⁴ <http://irsa.ipac.caltech.edu/applications/2MASS>

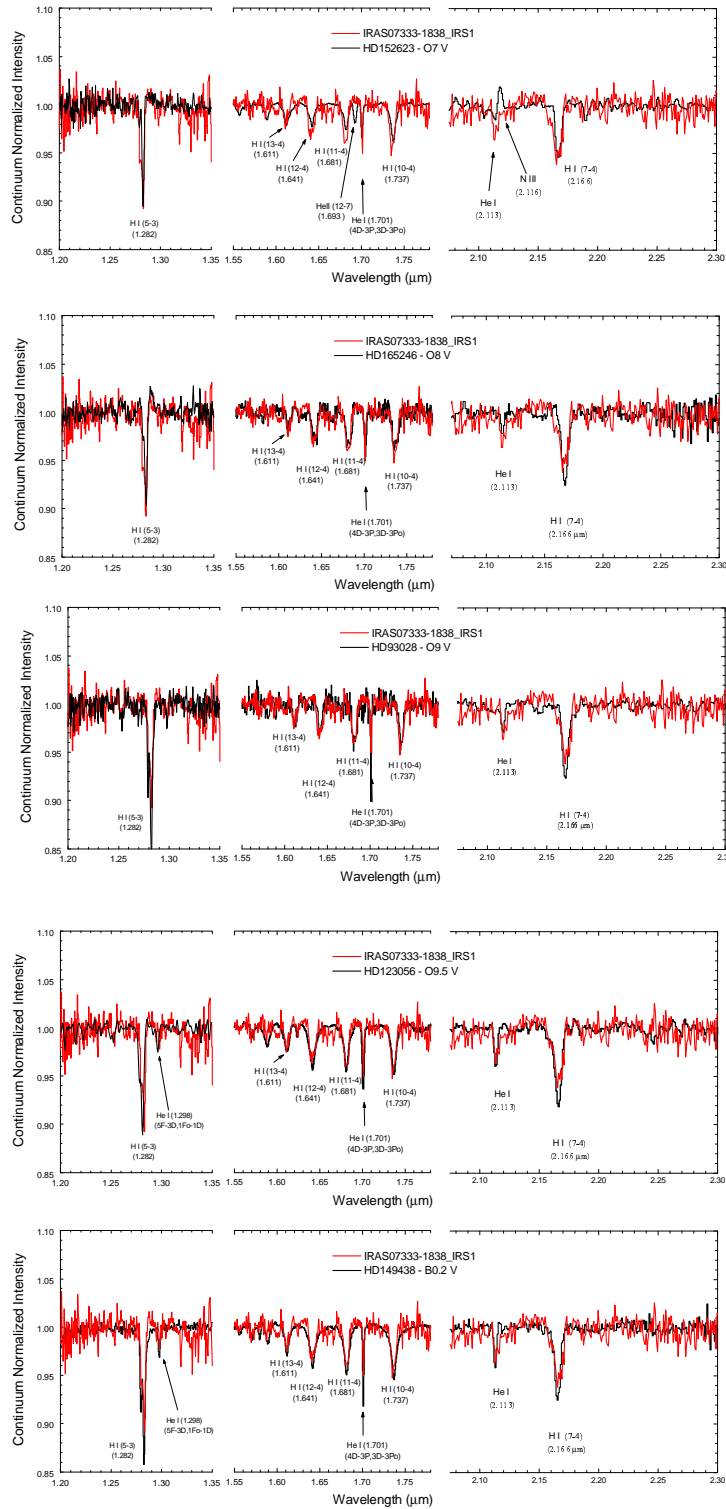


Figure 5. The NIR spectra of the IRS1, superimposed on the J-, H- and K-band spectra of the known OB stars, HD152623 (O7v), HD165246 (O8v), HD93028 (O9v), HD123056 (O9.5v) and HD149438 (B0.2v).

4 ANALYSES AND DISCUSSION

4.1 The spectral type of main cluster source

As already mentioned before, Hunter & Massey (1990) obtained optical spectroscopy data for a non-resolved source in the direction of the core of the Sh 2-307 HII region, classifying it as a B0v star. Thanks to the high-resolution NIR images obtained by the SOAR telescope, for the first time we resolved the sources in the central part of the HII region, separating the main ionizing agent of the cluster from its less luminous companion. In Figure 4 we show the R band image of the region (taken from the DSS archive), and the corresponding (at least for the central part) OSIRIS combined three colour image. One can see a large quantity of point sources in the inner part of the region, with IRS1 emerging as the brightest one. The K band image (represented in red) clearly shows the existence of a cavity inside the cloud, generated by the ionizing wind of the central source of the HII region.

In Figure 5 we present the IRS1 NIR spectra superimposed on that obtained for the five known OB stars (Maiz-Apellaniz et al., 2004, Hanson et al., 2005) present in **Table 1**. From the comparison of the IRS1 spectra with that of the templates stars, based on the presence and strength of the HeI lines, and the lack of HeII lines, we conclude that IRS1 probably is an O9v-O9.5v star.

The spectral type estimate we found for the main source in the region is only a bit different (in terms of sub-types) than that obtained by Hunter & Massey (1990). However, we notice that this small spectral type change imply in a significant difference in luminosity, with large impact in the quoted distance. In fact, the difference between visual absolute magnitudes of B0v and O9.5v stars, may be as high as 1.2 mag (Wegner 2006). Yet if we consider the case of zero age main-sequence stars (ZAMS), the differences in terms of absolute visual magnitudes drops to about 0.6-0.8 (Hanson et al. 1997), a value still considerable.

4.2 Spectrophotometric distance of the IRS1 source: An estimate for the cluster distance

From the spectral type estimate obtained in the previous section, and the NIR photometry, we are able to compute the distance to the main cluster source.

The NIR absolute magnitudes were computed using the intrinsic colours for early-O stars given by Koornneef (1983), and the absolute M_V magnitudes for ZAMS O9v and O9.5v stars given by Hanson et al. 1997. We choose to use the absolute magnitude values for ZAMS in order to be conservative in the distance determination. In fact, it is well known that ZAMS OB dwarfs found in very young clusters are less luminous than that found in the Galactic field (Hanson et al. 1997, Walborn 2002, Wegner 2006). The measured J , H and K magnitudes for IRS1 (presented in Table 1) are 10.66 ± 0.05 , 10.35 ± 0.06 and 10.21 ± 0.07 while its $(J - H)$ and $(H - K)$ colours are 0.31 ± 0.08 and 0.14 ± 0.09 , respectively. The mean intrinsic $(J - H)$ and $(H - K)$ colours for O9v-O9.5v stars are $(J - H)_0 = -0.12$ and $(H - K)_0 = 0.05$ (Koornneef 1983). The resulting mean colour excess are $E(J - H) = 0.43$ and $E(H - K) = 0.19$, which using the standard interstellar extinction law given by Fitzpatrick (1999)

correspond to $A_V = 3.6 \pm 0.7$ magnitudes or $A_J = 1.1 \pm 0.2$ and $A_K = 0.4 \pm 0.1$.

Using the appropriate values, we computed a distance of 3.2 ± 0.5 kpc, which for $R_0 = 8$ kpc, puts the Sh 2-307 HII region at more than 10 kpc from the Galactic centre. The quoted error in the value for the distance to IRS1 source was calculated taking into account the associated uncertainty in the extinction, photometry, and also the error that comes from the uncertainty on the absolute magnitude derived from the spectral type determination itself (for example, $M_J = -3.0$ for an O9v star and -2.85 for an O9.5v). As a last comment, we notice that in the scenario where IRS1 appears as a main-sequence star (e.g. not a ZAMS), the quoted distance would increase by about 1.1 kpc.

4.3 The stellar population of the Sh 2-307 HII region

4.3.1 The colour-colour diagram: A cluster of PMS stars

Useful information about the nature of the sources detected in the cluster region, can be obtained from the $J - H$ versus $H - K_s$ colour-colour (CC) diagram, shown in Fig.6. There we represented the non-reddened locus for main sequence, giants (Koornneef, 1983), and classical T-Tauri (CTT) stars (Meyer et al., 1997), together with the associated reddening vector lines, which follow the standard interstellar law taken from Fitzpatrick (1999). We can see that the bulk of the cluster sources are concentrated in a small region of the CC diagram, presenting colours in the range $0.95 \leq J - H \leq 1.4$ and $0.35 \leq H - K \leq 0.9$. The majority of the objects in this group are concentrated along the reddening vector band of the empirical CTT locus, indicating that the cluster stellar population is formed by a significant number of sources still in their pre-main sequence (PMS) evolutionary phase. This sources are identified in the last column of Table I as "CTT candidate".

4.3.2 Contamination by field stars

The contamination by Galactic field sources in the cluster stellar population, can be evaluate taking into account the magnitudes and colours of the sources detected in the control region.

From Fig.6, we notice that there is a group of sources occupying the lower-left part of the CC diagram, presenting colours in the range $0.2 \leq J - H \leq 0.6$ and $0.1 \leq H - K \leq 0.3$. Some of these objects can be true members of the cluster (the main ionizing source in the region belongs to this group), however in this particular case, the contamination by field stellar sources may be important. In fact, their location in the CC space coincides with that occupied by the majority of the sources detected in the control field (represented by the blue filled squares), which have small colours, as expected for a foreground Galactic stellar population. On the other hand, we can see from Fig.7 that the majority of the objects in the control region present colours in the range $0.1 \leq (H - K_S) \leq 0.35$, and magnitudes $J \geq 14.5$. On the other hand, we also notice that many objects present $H - K_S$ colours excess less than that for the reddened main sequence locus, indicating that they probably do not belong to the star formation region. The majority of the sources in

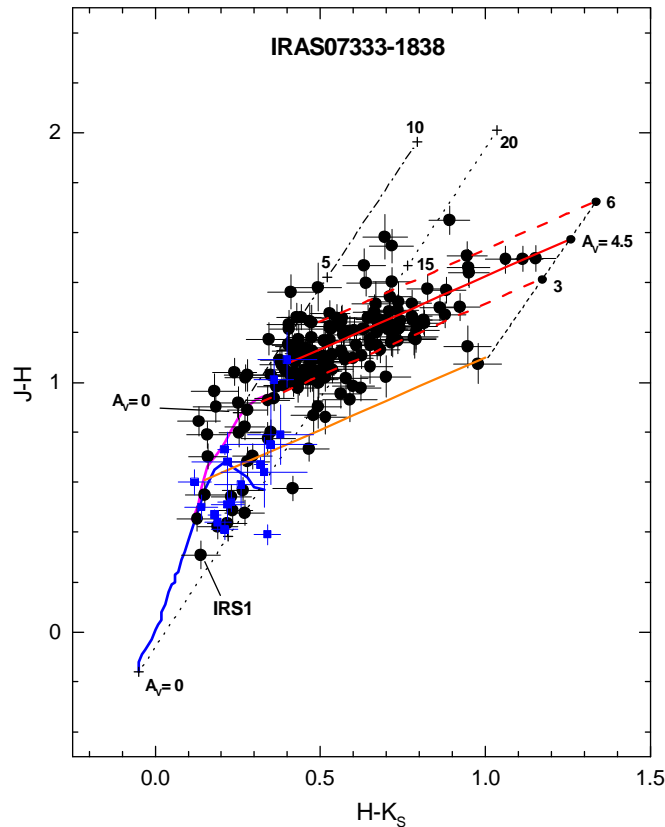


Figure 6. The $J - H$ versus $H - K_S$ diagram of the sources detected in the direction of IRAS07333-1838 source (represented by the black filled circles) and that from the control region (the blue filled triangles). The theoretical locus for the main-sequence stars is represented by the blue continuum line, while that for the giant branch (Koornneef, 1983) is represented by the pink continuum line. We also represented the non-reddened theoretical locus for the classical T-Tauri, by the orange line. The corresponding reddening vectors are indicate respectively by the dashed-dotted, dotted, and dashed lines. We also represented by red lines, the theoretical CTT locus reddened by 3, 4.5 and 6 magnitudes of visual extinction (Fitzpatrick, 1999).

this group are referred in Table I as "field source", indicating their status of probable non-cluster members.

4.3.3 Cluster mean visual extinction

Assuming that the sources presenting colours in the range $0.95 \leq J - H \leq 1.4$ and $0.35 \leq H - K \leq 0.7$ are CTT stars, and remembering that the T-Tauri locus was derived from modeling accretion disks (Meyer et al. 1997), we can estimate a value for the *mean visual extinction* to this group of cluster sources. From the interstellar extinction law of Fitzpatrick (1999), we applied the corresponding de-reddening vector to each source in these group, and found a mean value for A_V of about 4.5 ± 1.5 magnitudes. We can evaluate this result representing in Fig.6 (by red lines) the CTT locus reddened by 3, 4.5 and 6 magnitudes of visual extinction. One can see that the majority of the sources lie well in between the two extreme reddened CTT locus, which indicates that the extinction to the cluster members ranges between $A_V=3$, and $A_V=6$ magnitudes. The mean value $A_V=4.5$ mag is somewhat higher than that found from the photometry of the IRS1 source. The reason for this small difference probably is due to the fact that the

dust destruction process (generated by UV photons of the massive star), is more effective in the innermost part of the cluster, resulting in a lower visual extinction. This assumption is corroborate by the composite three colour image of the cluster core, shown in Fig.4. In fact, we can see that the central part of the cluster appears "cleaned" while other sources in the region seems to be involved by a tenuous extended emission, which probably is produced by scattered stellar light. Indeed, both results agree well when we take into account the associated uncertainty.

4.3.4 The colour-magnitude diagram

Additional information about the stellar population in the direction of the Sh 2-307 region can be obtained using the K_S versus $H - K_S$ colour-magnitude (CM) diagram. In Fig.7, we show the diagram constructed from the photometric data of the sources in Table 1. In all diagrams, the sources in the cluster region (that found simultaneously in the J , H and K_S bands), are represented by the black filled circles. As in the case of the CC diagram, the contamination by field stars in the cluster population can be evaluate from the blue filled squares (representing the objects de-

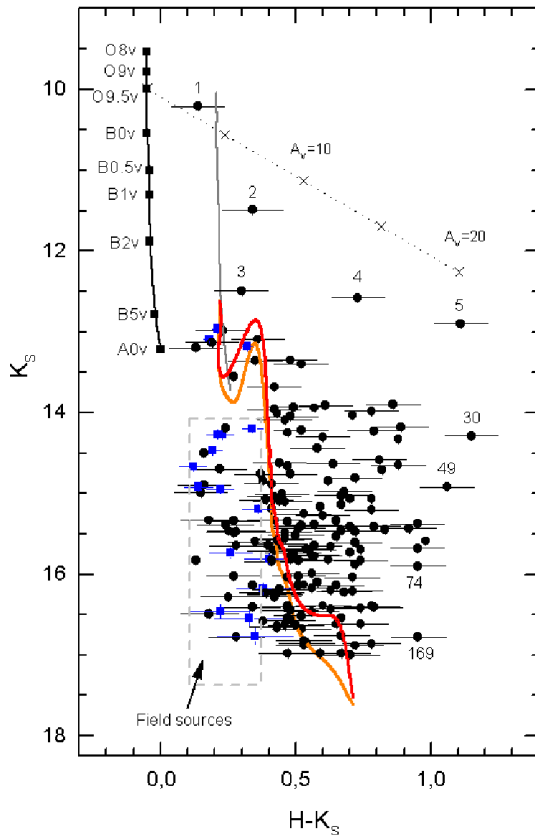


Figure 7. The J versus $H - K_s$ diagram. The sources from the cluster and control regions are represented by black filled circles, and blue filled squares, respectively. The locus for class v stars at 3.2 kpc and the positions corresponding to each spectral type from A0v till O8v, are indicated by the black continuum line. The reddening vector representing the standard interstellar reddening law (Fitspatrick, 1999), is indicated by the black dotted line. We also indicate by the gray line, the main-sequence reddened by $A_V=4.5$ magnitudes. The diagram also presents the 2 and 3 Myear PMS tracks (represented by the red and orange continuous lines, respectively), computed for masses in the range $0.1-7 M_\odot$ (Siess et al. 2000), distance of 3.2 kpc and interstellar absorption corresponding to $A_V=4.5$ mag.

tected in the control region). The locus for class v stars at 3.2 kpc was plotted, and the spectral types from A0v till O8v are indicated. The intrinsic colours were taken from Koornneef (1983), while the absolute J magnitudes were calculated from the absolute visual luminosity for the zero-age main sequence (ZAMS) taken from Hanson et al. (1997). The reddening vector for an O9.5v star is shown by the dashed line, and the positions corresponding to $A_V=5, 10, 15$ and 20 magnitudes (Fitspatrick, 1999), are indicated by crosses. For completeness, we also indicate by the gray line, the main-sequence locus reddened by $A_V = 4.5$ mag, the mean visual extinction inferred from the reddened CTT locus in the CC diagram.

It is interesting to notice that some of the excess emission sources are too bright to be individual low-mass and T-Tauri objects. For example, from the brightness and colours of the IRS4 and IRS5 and IRS30 sources, we suspect that as in the case of the IRS2 one, they are candidate to intermediate mass young stellar objects. Unfortunately, from the present dataset this is all we can say about such sources. In this sense, they are excellent targets for further near- and mid-IR spectrophotometric studies.

4.3.5 Age estimates for the cluster stellar population

One can determine the approximate age of a cluster population by comparing their observed magnitudes and colours with that from evolutionary stellar models. For very young stellar clusters, one method consists in to study the post-main sequence evolution of the earliest members (if significant evolution has occurred). In this sense, we can initially assume the main sequence life time of O9v-9.5v stars of about 5 Myrs (Meynet et al. 1994; Palla & Stahler 1999) as an upper limit for the cluster age. On the other hand, one can also infer the age of the stellar population by fitting the low-mass pre-main sequence members using theoretical isochrones. Fitting PMS isochrones to young stellar clusters is still an uncertain process, mainly for stellar ages less than 1 Myrs (Baraffe et al. 2002). Indeed its usage is certainly useful to obtain estimates for the cluster age, and in the case of non-coeval stellar populations, to get an idea of their relative ages.

In order to perform the isochrones fit to the cluster sources, we show in the K_s versus $H - K_s$ CM diagrams (Fig. 7), the 2 and 3 Myear PMS tracks (represented by the red and orange continuous lines, respectively), computed

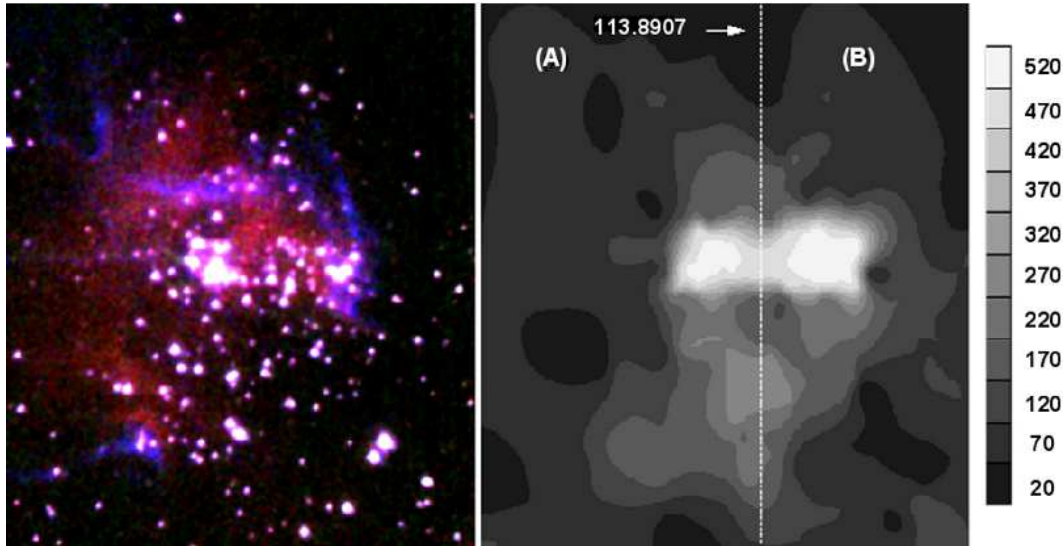


Figure 8. (left) The three colour composite image made from the Br γ (red), Continuum (Green) and H $_2$ (Blue) frames. North is to the Top, east to the left, and the field of view is about $70'' \times 60''$. (right) The magnitude limited ($K_S < 15.5$) surface density distribution of sources in the cluster region. The contours start from a surface density of 20 sources pc^{-2} till a maximum of 520 sources pc^{-2} . The white dotted line divide the cluster field in two regions (A) and (B), in which is performed the study of excess emission sources.

for $Z=0.02$ and masses in the range $0.1-7 M_{\odot}$ (Siess et al. 2000). The K_s -band magnitudes were computed for a distance of 3.2 kpc and the colours were reddened by $A_V=4.5$ mag (Fitspatrick, 1999), the mean visual extinction inferred from the CTTS locus (see Fig.6). As already discussed in the analyses made for the CC diagram, the contamination by Galactic field stars must be small. The probable non-cluster members are the low luminosity objects that present magnitude and colours similar to that indicated by the blue square symbols (representing the sources detected in the control region). The probable exceptions are the brightest cluster candidates that are well placed in the core of the cluster region (as is the case of the IRS1 source).

From the comparison of the early-type sources in the CM diagram ($0.2 \leq H - K_s \leq 0.5$ and $K_s \sim 13.5$) with the PMS evolutionary tracks, we can see that the main-sequence (MS) turn-on of the cluster probably is occurring for the 2-3 Myrs old sources corresponding to ZAMS stars of 3-3.5 M_{\odot} . This is an important information that indicates the probable age of the O star. Another useful feature that seems to indicate the presence of a 2-3 Myrs old stellar population, comes from an inspection of the low mass end of the cluster source distribution. We can notice that the oldest PMS tracks "fit" well the left boundary of the cluster source sample, including the "knee" at the 0.3-0.5 M_{\odot} range. On the other hand, we also can see that there are a large quantity of objects farthest to the right (much more than 1.5 magnitudes) of the *reddened* PMS track locus. Such sources present strong excess emission in the K-band, a feature that amplify the broadening of the distribution of these sources in the colour-magnitude space.

Another possible explanation for the broad distribution of sources in the CM space, can be obtained if we assume that the cluster stellar population is formed by sources in different evolutionary stages. In this sense, the observed scatter could be due to a combination of photometric uncertainty,

small differential reddening and an age spread of several hundred thousand years. Evidence indicating the presence of an age spread on the stellar population may come from the comparison of the 2 Myr PMS model with the low mass end of the source cluster distribution. In this case, we can see that several low luminosity sources are reasonably well fitted by the low-mass end of the 2 Myrs PMS track, which however is not true when we consider the brightest and reddest objects. Even the use of a younger PMS model (like the 1 and 0.5 Myrs one) does not result in reasonable fit to the reddest sample and the reason for that probably is the fact that the SEDs predicted by the PMS models result only from the contracting photospheres on the Hayashi tracks (vertical tracks in the CM diagrams), ignoring the effects produced by the presence of accreting disks. The NIR excess generated by accretion disks would explain (in principle) why these sources appears red-wards of the predicted PMS isochrones.

An important cluster parameter related with the presence of disks, is the frequency of cluster members that show NIR excess emission, and its relation with the age of the cluster stellar population. In fact, the initial disk frequency and the variation of the cluster-disk frequency with the cluster age, sets the timescale for both, the disk evolution and the lifetime of the circumstellar disk phase (Lada et al. 2000, Lada & Lada 2003). Haisch, Lada & Lada (2001) found that the disk fraction rapidly drops with the cluster age. They conclude that for a one-million year cluster age, the disk fraction is about 80 percent, dropping to only 10 percent for a five million years cluster age. In this sense, the direct measurement of the cluster disk frequency (inferred from the fraction of sources showing excess emission) enable us to estimate the clusters age. The fraction obtained from the J-, H- and K-bands observations can be considered a lower limit for the true number of sources with excess emission in a cluster. This is because some fraction of sources that do

have accreting disks, may show JHK colours similar to that presented by reddened early- and late-type "normal" stars. On the other hand, virtually all sources in a cluster that have accreting disks, may be identified in a JHKL diagram where this degenerence is broken (Lada et al. 2000).

We can obtain another estimated for the mean age of the cluster stellar population, by computing the fraction of sources showing excess emission in the *JHK* colour-colour diagram, and comparing the result with those obtained by Lada et al.(2000), and Haisch, Lada & Lada (2001). **In order to be conservative and to avoid any bias generated by incompleteness sample effects (for example due to the lack of completeness correction in some crowded parts of the cluster region), we will consider only the sources located to the right of the redenning vector for early type sources that have K_S magnitudes < 15.5 , a value that is more than one magnitude less than the derived completeness limit for the K_S band (16.7).** There are 86 sources in Table 1 with $K_S < 15.5$ (those detected simultaneously in the three NIR bands) with 14 being probable galactic field sources, and 27 presenting K-band excess emission, which corresponds to a fraction of $38 \pm 8\%$. If we assume that the majority of the sources in our sample are less massive than a B star (a reasonable assumption considering the large quantity of T-Tauri star candidates found in this cluster), we can use the results obtained by Lada et al.(2000) to estimate (from their Table 2) as about 60% the probable true fraction of excess emission sources in this cluster, which corresponds to an age of 2.5 Myrs (Haisch, Lada & Lada 2001), in good agreement with the value derived from the use of PMS evolutionary tracks in the colour-magnitude diagram.

4.3.6 Evidence for triggered star formation

Triggered star formation is a process powered by ionization and/or shock fronts generated by massive stars. It is believed to occurs at the interface between the HII region and associated molecular cloud, and in this context, two main mechanisms have been proposed: The *radiation-driven implosion* and the *collect-and-collapse* models. In the first model, the expanding ionization front compresses the existing molecular clumps, leading to density enhancements, which eventually exceeds the local critical mass, collapsing to form new stars (Lefloch & Lazareff 1994). In the collect-and-collapse model, the neutral material accumulates between the ionization front of the HII region and the shock front in the neutral gas. This compressed material may be dynamically unstable on a short internal crossing timescale, forming cometary globules, which eventually will lead to the formation of massive fragments forming new generations of stars and/or clusters (Elmegreen & Lada 1977; Garcia-Segura & Franco 1996).

We searched for signs of triggered star formation, by initially studying the observed surface density distribution of sources, and their correlation with the extended emission in the region. In Figure 8 (left), we present the three colour combined image constructed from the $\text{Br}\gamma$ ($2.166\mu\text{m}$ - red), H_2 ($2.12\mu\text{m}$ - blue) and Continuum ($2.14\mu\text{m}$ - green) narrow band filter images. Combining these images together in this way allow us to visualise any spatial correlation between the point sources and observed extended emission, as well as, the

effects of the presence of the massive star in the surrounding medium, with the H_2 emission tracing the photo-dissociation regions (PDRs), and the $\text{Br}\gamma$ image tracing the ionized gas. In the case of the H_2 emission, we notice that it is strong to the north and to the west, but is absent to the east, indicating that in this direction most of the molecular gas probably was already dissociated by the UV photons of the O star. On the other hand, the $\text{Br}\gamma$ emission suddenly diminish to the south and southwest, indicating the presence of neutral gas.

The surface density distribution of the cluster sources reveals other interesting features. In Figure 8 (right), we show the magnitude limited ($K_S < 15.5$) surface density distribution of objects in the cluster region. We can see two prominent concentrations there. As expected, the O star (far the most massive source in the region) is related to the concentration that lies close to the geometrical centre of the cluster and associated HII region. On the other hand, the striking result is the presence of a second compact group of sources, which shows close spatial correlation with the strong H_2 photo-dissociation regions seem to the right of the extended $\text{Br}\gamma$ emission, apparently forming a sub-cluster. Finally, and as a last comment in this subject, there is a third less prominent sub-structure seem to the south of the main source. It extends till a small group of objects, associated with the H_2 emission seem in the left corner of the image in Figure 8 (left).

Interestingly, the features above described, agree with the scenarios predict by the two main triggering star formation process mentioned earlier. In fact, in the regions where the sources appear associated with the H_2 extended emission (the second compact group), the star formation would be occurred accordingly to the radiation-driven implosion model, while in the case of the sources that appears more embedded in the parental molecular cloud (like the sources associated with the third less prominent substructure to the south of IRS1, far away from the HII region ionization front), the collect-and-collapse model seems to be the most probable.

However, in order to properly support this assumption it is necessary to find some evidence for an age spread on the cluster stellar population. We did this by studding the fraction of sources in two cluster areas, as described as follow. From Figure 8 (right) we computed the fraction of sources showing excess emission in two separate regions (A) and (B), as indicated by the vertical dotted line, which corresponds to the sources found to the left and right from the R.A. coordinate 113.8907 (07:35:33.8). As already noted before, there are 86 sources in the cluster region presenting K_S magnitudes less than 15.5, with 47 (9 field sources) located in region (A) and 39 (5 field sources) in region (B). The total number of excess sources is 27, 11 from region (A) and 16 from region (B), which correspond to excess emission fractions of 29% and 47% respectively. This result indicates that the sources in region (B) probably are younger (as a sample) than that found in region (A).

The large number of low to intermediate mass YSO and T-Tauri candidates concentrated at specific distances from the main cluster source, their apparent spatial correlation with the H_2 emission, and the evidence of an age spread in the cluster population, are constrains that favor the assumption of triggered star formation in the region.

4.4 The Sh 2-307 HII region

From Figure 8(a) one can see that the Br γ extended emission has a nearly spherical shape centred on IRS1. We can estimate the size of the Sh 2-307 HII region by measuring the angular diameter of the Br γ extended emission, which occurs in both, in the north-south and in the east-west directions. It measures about 60 arcsec that for a distance of 3.2 ± 0.5 kpc corresponds to $d \sim 0.94\pm 0.15$ pc.

The numerical density of the ionized gas can be derived from the emission measure, which can be computed from the detected 5 GHz flux density and measured angular diameter, assuming that the emitting region has an spherical shape. In the calculation, we used the expression for the expected free-free emission from an optically thin plasma at wavelength λ , given by:

$$S_\nu = 5.4 \times 10^{-16} g_{ff}(\lambda, T) \Omega E T^{-1/2} e^{-hc/\lambda kT} \text{ Jy} \quad (1)$$

where E is the emission measure (cm^{-5}), Ω is the solid angle of the source and $g_{ff}(\lambda, T)$ is the Gaunt factor, which for radio wavelengths can be computed from:

$$g_{ff}(\lambda, T) = \frac{\sqrt{3}}{\pi} \left[17.7 + \ln \left(\frac{T^{3/2} \lambda}{c} \right) \right] \quad (2)$$

Assuming $T=7500\text{K}$, $D=3.2$ kpc and $S_\nu=0.73$ Jy we found $E = 3.7 \times 10^{23} \text{cm}^{-5}$, which corresponds to a mean electron density $n_e \sim 550 \text{cm}^{-3}$. It is interesting to notice that the values of the diameter and electron density we found are in good agreement with the density-size relation derived by Kim & Koo (2001).

The diameter we found for the HII region indicates that Sh 2-307 had already evolved from the ultra-compact phase (when $d \leq 0.1$ pc), being in a more advanced evolutionary stage. We can estimate the age of Sh 2-307, assuming that it reached its *initial* Strongren radius in a very short time of a few 10^4 years (corresponding to a rapidly expansion phase dominated by the R-type shock - Spitzer 1978), and that after this phase, it has been expanding in a uniform medium owing to the pressure difference between the hot ionized gas and the outer cool molecular gas. This corresponds to a condition where the HII region expansion is governed by a weak D-type ionization front, with a rate of expansion that can be estimate using the equation (Spitzer 1978):

$$R_f(t) = R_i \left(1 + \frac{7C_{II}t}{4R_i} \right)^{4/7} \quad (3)$$

where R_i and R_f are the initial and final values for the Strongren radius, and C_{II} is the sound speed ($\sim 4\text{km/s}$) in the HII region. In the calculation we assumed that the numerical density in the beginning of the ultra-compact phase was about 10^5cm^{-3} (Churchwell, 2002). The initial Strongren radius for an O9V-9.5V star ($N_{Ly}=7.9 \times 10^{47} \text{s}^{-1}$, Martins et al. 2005) is $R_i \sim 0.012$ pc and considering $R_f=0.47$ pc, we found an age of about $(1.6\pm 0.4) \times 10^6$ years. Despite the uncertainty due to the assumption of uniform medium and because the velocity of expansion probably changes with time, the derived value probably is a reasonable estimation for the age of the HII region, considering that it had already evolved from the UC phase, and probably is still expanding, as suggested by the presence of PDRs.

From the observed 5GHz flux density we can obtain another independent estimate for the heliocentric distance

of the HII region. In the calculation we used the relation between N_{Ly} and S_ν given by Urquhart et al. (2004),

$$N_{Ly} = 7.7 \times 10^{43} S_\nu D^2 \nu^{0.1} \text{s}^{-1} \quad (4)$$

with S_ν in mJy, D in kpc and ν in GHz. For $N_{Ly}=7.9 \times 10^{47} \text{s}^{-1}$ and $S_\nu=730$ mJy, we compute a distance of about 3.5 kpc, in good agreement with the spectrophotometric result of 3.2 ± 0.5 kpc. This result can be considered an *upper limit* considering that some fraction of the Lyman continuum photons produced by the O star certainly are "lost" due to dust absorption or by escaping from the region. From this result we estimate as $\sim 85\%$ the fraction of Lyman continuum photons generated by the massive star that effectively ionizes the gas in the HII region.

5 SUMMARY

In this work we performed a detailed study of the Sh 2-307 HII region, and associated stellar population. From the high quality SOAR-OSIRIS NIR broad-band images, we were able to resolve the sources placed in the innermost zones, identifying the ionizing agent of the HII region detected at optical and radio wavelengths. The analyses of the J-, H- and K-band OSIRIS spectrophotometric data of this object, enable us to classify it as an O9V-O9.5V star, reddened by $A_V = 3.6 \pm 0.7$ magnitudes. It is probably placed at a heliocentric distance of 3.2 ± 0.5 kpc that for $R_0 = 8$ kpc, puts the Sh 2-307 HII region at more than 10 kpc from the Galactic centre.

There are 179 NIR objects in an area of about 1.2×1.2 square arcmin, the majority of them presenting colours characteristic of T-Tauri sources. From the comparison of the early-type sources in the CM diagram with the PMS evolutionary tracks, we found that the main-sequence turn-on is probably occurring for sources 2-3 Myrs old, which correspond to 3-3.5 M_\odot ZAMS stars. Considering the brightness and colours of the IRS2, IRS4 and IRS5 sources, we suspect that they probably are intermediate mass young stellar objects. A constrain that provides some support for this assumption, is the detection of CO band absorption lines in the NIR spectra of the IRS2 source, a feature commonly found in intermediate-mass YSOs.

The narrow-band Br γ image shows that the HII region has an spherical like shape with a mean radius of about 0.47 ± 0.15 pc, indicating that it had already evolved from the ultra-compact phase. From the 5 GHz flux density taken from the PMN catalogue, and the measured radius, we estimate a mean electron density of 550cm^{-3} and an HII region age of about 1.6×10^6 years. The PDRs at the interface between the ionized and molecular gas, are well traced by the H $_2$ emission detected in the narrow band images. The spatial correlation between the ionized gas, and the PDRs (clearly seem to the north and to the west of the ionizing source) lead us to conclude that there is a high degree of interaction of the UV photons from the O star with the nearby molecular cloud, suggesting that the HII region probably is still expanding into the surrounding medium. On the other hand, there is no H $_2$ emission to the east, indicating the absence of molecular gas in this part of the region. Indeed, we detect strong Br γ emission there, and considering its interaction with small H $_2$ emitting "clumps" well seem

to the north and to the south, we conclude for the presence of a "champagne flow" occurring at the border of the parental molecular cloud, powered by the ionization front of the associated HII region. This conclusion agrees with the assumption made by Russeil et al. (1995), who suggested that a "champagne flow" in the region would produce the observed discrepancy in the corresponding HII region radial velocity, inferred from their H α Fabry-Perot observations. Finally, based on the analyses of the relative fraction of excess emission sources in the region, and the observed spatial distribution of low-mass YSO and T-Tauri stars relative to the main cluster source, we conclude that the O star probably has been triggering the star formation process in the region.

ACKNOWLEDGEMENTS

We would like to thank the comments and suggestions made by the anonymous referee. Her/his comments were very useful to improve the quality and presentation of the final manuscript. This work was partially supported by the ALMA-CONICYT Fund, under the project number 31060004, "A New Astronomer for the Astrophysics Group, Universidad de La Serena", and by the Physics department of the Universidad de La Serena. We acknowledge the staff of the SOAR Telescope for their efficient support during the observations. This publication makes use of data products from the Two Micron All Sky Survey, which is a joint project of the University of Massachusetts and the Infrared Processing and Analysis Center/California Institute of Technology, funded by the National Aeronautics and Space Administration and the National Science Foundation. This work was partially supported by the Brazilian agency FAPESP.

REFERENCES

- Ali, B., Carr, John S., Depoy, D. L., Frogel, Jay A., Sellgren, K., 1995, AJ, 110, 2415
 Baraffe, I., Chabrier, G., Allard, F., Hauschildt, P. H., 1998, A&A, 337, 403
 Balog, Z., Kenyon, S. J., Lada, E. A., Barsony, M., Vinko, J., Gaspar, A., 2004, AJ, 128, 2942
 Blum, R. D., Ramond, T. M., Conti, P. S., Figer, D. F., 1997, AJ, 113, 1855
 Burrows, A., et al. 1997, ApJ, 491, 856
 D'Antona, F., & Mazzitelli, I. 1994, ApJS, 90, 467
 Evans, N.J., 1999, ARAA, 37, 311
 Salpeter, E.E., 1955, ApJ, 121, 161
 Scalo, J., 1986, Fund. Cosmic Phys. 11: 1-278
 Shu, F.H., Adams, F.C., Lizano, S., 1987, ARAA, 25, 23
 Fitzpatrick E.L., 1999, PASP, 111, 63
 Haisch, Karl E., Jr., Lada, Elizabeth A., Lada, Charles J., 2001, ApJ, 553L, 153
 Han, F., Mao, R.Q., Lu, J., Wu, Y.F., Sun, J., Wang, J.S., Pei, C.C., Fan, Y., Tang, G.S. & Ji, H.R., 1998, A&AS, 127, 181
 Hanson, M.M., Conti, P.S. & Rieke, M.J., 1996, ApJS, 107, 281
 Hanson, M. M., Howarth, I. D., Conti, P.S., 1997, ApJ, 489, 698
 Hanson M.M., Kudritzki, R.-P.; Kenworthy, M. A.; Puls, J.; Tokunaga, A. T., 2005, ApJS, 161, 154
 Hunter, D. A., Massey, P., 1990, AJ, 99, 846
 Ivanov, V.D., Rieke, M.J., Engelbracht, C.W., Alonso-Herrero, A., Rieke, G.H., Luhman, K.L., 2004, ApJS, 151, 387
 Kenyon, S. J. & Hartmann, L., 1995, ApJS, 101, 117K
 Koornneef, J., 1983, A&A, 128, 84
 Lada, E., A., Lada, C. J., 1995, AJ, 109, 1682
 Lada, C. J., Muench, A. A., Haisch, K. E., Jr., Lada, E. A., Alves, J. F., Tollestrup, E. V., Willner, S. P., 2000, AJ, 120, 3162
 Haisch, K. E., Jr., Lada, E. A., Lada, C. J., 2001, ApJ, 553L, 153
 Lada, C.J., Lada, E.A., 2003, ARAA, 41, 57
 Livingston, W., Wallace, L., 1991, N.S.O. Technical Report 91-001
 Martins, F., Schaerer, D., Hillier, D. J., 2005, A&A, 436, 1049
 Massey, P., 2003, ARAA, 41, 15
 McKee, C.F. & Ostriker, E.C., 2007, ARAA, 45, 565
 Maiz-Apellaniz, J. & Walborn, N. R., 2004, ApJS, 151, 103
 Meyer, M. R., Calvet, N., Hillenbrand, L. A., 1997, AJ, 114, 288
 Meynet, G., Maeder, A., Schaller, G., Schaerer, D., Charbonnel, C., 1994, A&AS, 103, 97
 Moffat, A. F. J., Fitzgerald, M., P., Jackson, P. D., 1979, A&AS, 38, 197
 Palla, F., & Stahler, S. W., 1999, ApJ, 525, 772
 Prosser, C., Stauffer, J. R., Hartmann, L., Soderblom, D., Jones, B. F., Werner, M. W., McCaughrean, M. J., 1994, ApJ, 421, 517
 Robitaille, T. P., Barbara A. Whitney, Remy Indebetouw, Kenneth Wood, and Pia Denzmore, 2006, ApJs, 167, 256
 Roman-Lopes A., Abraham Z. & Lépine J.R.D., 2003, AJ, 126, 1896
 Roman-Lopes A., Abraham Z., 2004, AJ, 127, 2817
 Russeil, D., Georgelin, Y. M., Georgelin, Y. P., le Coarer, E., Marcelin, M., 1995, A&AS, 114, 557
 Sharpless, S., 1959, ApJS, 4, 257
 Siess, L., Dufour, E., & Forestini, M., 2000, A&A, 358, 593
 Spitzer, L., 1978, Physical processes in the interstellar medium, New York Wiley-Interscience
 Stetson, P. B., 1987, PASP, 99, 191S
 Tenorio-Tagle, 1979, A&A, 71, 59
 Walborn, N.R., 2002, AJ, 124, 507
 Wegner, W., 2006, MNRAS, 371, 185
 Wood D.O.S. & Churchwell E., 1989, ApJ, 340, 265

Table 1. The list of known OB stars used as templates.

ID	SpType
HD149438	B0.2v
HD123056	O9.5v
HD93028	O9v
HD165246	O8v
HD152623	O7v

Table 2. The J , H and K_S OSIRIS photometry of the sources detected in the direction of SH 2-307 HII region (part 1).

IRS	RA (J2000)	Dec (J2000)	J	H	K	Note	NIR K-band excess?
1	113,8924	-18,7597	10,66 ± 0,05	10,35 ± 0,06	10,21 ± 0,07	O9v-O9.5v	
2	113,8847	-18,7669	12,60 ± 0,05	11,83 ± 0,07	11,49 ± 0,09	YSO candidate	
3	113,8863	-18,7597	13,49 ± 0,05	12,78 ± 0,06	12,49 ± 0,08	B2v	
4	113,8852	-18,7675	14,48 ± 0,05	13,31 ± 0,06	12,58 ± 0,08	YSO candidate	yes
5	113,8913	-18,7665	15,51 ± 0,05	14,01 ± 0,06	12,90 ± 0,08	YSO candidate	yes
6	113,8934	-18,7593	13,75 ± 0,05	13,21 ± 0,06	12,98 ± 0,08	B5v	
7	113,8943	-18,7629	14,39 ± 0,05	13,45 ± 0,06	13,09 ± 0,08	T-Tauri candidate	
8	113,8865	-18,7696	13,74 ± 0,05	13,31 ± 0,06	13,13 ± 0,08	B5v-B8v	
9	113,9019	-18,7542	13,78 ± 0,05	13,33 ± 0,06	13,20 ± 0,08	field source	
10	113,8827	-18,7686	14,88 ± 0,05	13,83 ± 0,06	13,35 ± 0,08	T-Tauri candidate	
11	113,8918	-18,7660	14,51 ± 0,05	13,71 ± 0,06	13,36 ± 0,08	field source	
12	113,8932	-18,7585	15,01 ± 0,05	13,93 ± 0,06	13,40 ± 0,08	T-Tauri candidate	
13	113,8885	-18,7706	14,31 ± 0,05	13,83 ± 0,06	13,56 ± 0,08	T-Tauri candidate	
14	113,8965	-18,7645	15,24 ± 0,05	14,10 ± 0,06	13,68 ± 0,08	T-Tauri candidate	
15	113,8933	-18,7637	16,06 ± 0,05	14,76 ± 0,06	13,90 ± 0,08	T-Tauri candidate	yes
16	113,8918	-18,7641	15,67 ± 0,05	14,52 ± 0,06	13,91 ± 0,08	T-Tauri candidate	
17	113,8915	-18,7599	15,33 ± 0,08	14,42 ± 0,07	13,93 ± 0,08	T-Tauri candidate	
18	113,8874	-18,7589	15,72 ± 0,05	14,52 ± 0,06	13,94 ± 0,08	T-Tauri candidate	
19	113,8951	-18,7598	14,95 ± 0,05	14,38 ± 0,06	13,96 ± 0,08	T-Tauri candidate	yes
20	113,8923	-18,7574	16,02 ± 0,05	14,76 ± 0,06	13,98 ± 0,08	T-Tauri candidate	yes
21	113,8889	-18,7604	15,70 ± 0,05	14,44 ± 0,06	14,01 ± 0,08	T-Tauri candidate	
22	113,8878	-18,7631	15,95 ± 0,05	14,74 ± 0,06	14,03 ± 0,08	T-Tauri candidate	yes
23	113,8922	-18,7587	15,56 ± 0,06	14,53 ± 0,07	14,05 ± 0,08	T-Tauri candidate	
24	113,8870	-18,7596	15,58 ± 0,05	14,54 ± 0,06	14,09 ± 0,08	T-Tauri candidate	
25	113,8859	-18,7591	16,72 ± 0,05	15,07 ± 0,06	14,18 ± 0,08	T-Tauri candidate	yes
26	113,8881	-18,7521	14,91 ± 0,05	14,42 ± 0,06	14,19 ± 0,08	field source	
27	113,8929	-18,7585	15,76 ± 0,05	14,74 ± 0,06	14,22 ± 0,08	T-Tauri candidate	
28	113,8910	-18,7609	16,24 ± 0,05	15,02 ± 0,06	14,23 ± 0,08	T-Tauri candidate	yes
29	113,8892	-18,7610	15,45 ± 0,05	14,71 ± 0,06	14,25 ± 0,08	T-Tauri candidate	yes
30	113,8937	-18,7713	16,94 ± 0,05	15,44 ± 0,06	14,29 ± 0,08	YSO candidate	yes
31	113,8941	-18,7637	16,00 ± 0,05	14,9 ± 0,06	14,3 ± 0,08	T-Tauri candidate	
32	113,8889	-18,7601	16,48 ± 0,05	15,21 ± 0,06	14,33 ± 0,08	T-Tauri candidate	yes
33	113,8924	-18,7610	16,11 ± 0,05	15,02 ± 0,06	14,44 ± 0,08	T-Tauri candidate	
34	113,8898	-18,7600	15,44 ± 0,05	14,65 ± 0,06	14,50 ± 0,08	field source	
35	113,8918	-18,7586	16,65 ± 0,05	15,40 ± 0,06	14,58 ± 0,08	T-Tauri candidate	yes
36	113,8932	-18,7668	16,19 ± 0,05	15,06 ± 0,06	14,62 ± 0,08	T-Tauri candidate	
37	113,8939	-18,7490	16,67 ± 0,05	15,27 ± 0,06	14,63 ± 0,08	field source	
38	113,8948	-18,7540	16,90 ± 0,05	15,53 ± 0,06	14,65 ± 0,08	T-Tauri candidate	yes
39	113,8894	-18,7550	16,18 ± 0,05	15,12 ± 0,06	14,66 ± 0,08	T-Tauri candidate	
40	113,8959	-18,7617	15,35 ± 0,05	14,92 ± 0,06	14,70 ± 0,08	field source	
41	113,8900	-18,7635	16,76 ± 0,05	15,53 ± 0,06	14,71 ± 0,08	T-Tauri candidate	yes
42	113,8811	-18,7605	16,34 ± 0,05	15,24 ± 0,06	14,76 ± 0,08	T-Tauri candidate	
43	113,8943	-18,7606	16,11 ± 0,05	15,13 ± 0,06	14,76 ± 0,08	T-Tauri candidate	
44	113,8830	-18,7626	16,68 ± 0,05	15,52 ± 0,06	14,81 ± 0,08	T-Tauri candidate	yes
45	113,8884	-18,7594	16,57 ± 0,05	15,46 ± 0,06	14,84 ± 0,08	T-Tauri candidate	yes
46	113,8902	-18,7639	16,32 ± 0,05	15,23 ± 0,06	14,85 ± 0,08	T-Tauri candidate	
47	113,8970	-18,7645	16,50 ± 0,05	15,29 ± 0,06	14,88 ± 0,08	T-Tauri candidate	
48	113,9015	-18,7653	15,77 ± 0,05	15,06 ± 0,06	14,90 ± 0,08	field source	
49	113,8924	-18,7625	17,48 ± 0,05	15,98 ± 0,06	14,92 ± 0,08	T-Tauri candidate	yes
50	113,8831	-18,7564	16,79 ± 0,05	15,67 ± 0,06	14,98 ± 0,08	T-Tauri candidate	yes
51	113,9016	-18,7631	15,69 ± 0,05	15,14 ± 0,06	14,99 ± 0,08	field source	
52	113,8949	-18,7646	16,51 ± 0,05	15,46 ± 0,06	15,01 ± 0,08	T-Tauri candidate	
53	113,8928	-18,7600			15,03 ± 0,17		
54	113,8939	-18,7651	16,95 ± 0,05	15,70 ± 0,06	15,03 ± 0,08	T-Tauri candidate	
55	113,8929	-18,7616	16,45 ± 0,05	15,46 ± 0,06	15,04 ± 0,08	T-Tauri candidate	
56	113,8905	-18,7541	17,09 ± 0,05	15,84 ± 0,06	15,06 ± 0,08	T-Tauri candidate	yes
57	113,8892	-18,7621	17,00 ± 0,05	15,75 ± 0,06	15,06 ± 0,08	T-Tauri candidate	yes
58	113,8890	-18,7551	16,52 ± 0,05	15,48 ± 0,06	15,06 ± 0,08	T-Tauri candidate	
59	113,8870	-18,7611	16,46 ± 0,05	15,47 ± 0,06	15,08 ± 0,08	T-Tauri candidate	
60	113,8998	-18,7679	16,80 ± 0,05	15,53 ± 0,06	15,09 ± 0,08	T-Tauri candidate	

Table 3. The J , H and K_S OSIRIS photometry of the sources detected in the direction of SH 2-307 HII region (part 2).

IRS	RA (J2000)	Dec (J2000)	J	H	K	Note	NIR K-band excess?
61	113,8860	-18,7604	16,61 ± 0,05	15,56 ± 0,06	15,10 ± 0,08	T-Tauri candidate	
62	113,8881	-18,7569	16,97 ± 0,05	15,82 ± 0,06	15,14 ± 0,08	T-Tauri candidate	yes
63	113,8898	-18,7595	16,96 ± 0,05	15,75 ± 0,06	15,16 ± 0,08	T-Tauri candidate	
64	113,8916	-18,7664	16,83 ± 0,05	15,60 ± 0,06	15,19 ± 0,08	T-Tauri candidate	
65	113,8821	-18,7599	17,29 ± 0,05	15,98 ± 0,06	15,20 ± 0,08	T-Tauri candidate	yes
66	113,8944	-18,7596	17,05 ± 0,05	15,78 ± 0,06	15,25 ± 0,08	T-Tauri candidate	
67	113,8852	-18,7631	17,08 ± 0,05	15,88 ± 0,06	15,27 ± 0,08	T-Tauri candidate	
68	113,8865	-18,7600	16,47 ± 0,06	15,51 ± 0,07	15,33 ± 0,08	field source	
69	113,8959	-18,7669			15,33 ± 0,08		
70	113,8937	-18,7604	16,78 ± 0,05	15,75 ± 0,06	15,33 ± 0,08	T-Tauri candidate	
71	113,8932	-18,7675	16,63 ± 0,05	15,61 ± 0,06	15,34 ± 0,08	field source	
72	113,8873	-18,7696	17,25 ± 0,05	15,99 ± 0,06	15,34 ± 0,08	T-Tauri candidate	
73	113,8878	-18,7654	16,90 ± 0,05	15,82 ± 0,06	15,35 ± 0,08	T-Tauri candidate	
74	113,8979	-18,7693	17,83 ± 0,05	16,32 ± 0,06	15,38 ± 0,08	T-Tauri candidate	yes
75	113,8915	-18,7640	16,67 ± 0,05	15,63 ± 0,06	15,39 ± 0,08	field source	
76	113,8935	-18,7674	17,21 ± 0,05	15,96 ± 0,06	15,39 ± 0,08	T-Tauri candidate	
77	113,8912	-18,7600	16,78 ± 0,06	15,92 ± 0,06	15,40 ± 0,08	T-Tauri candidate	yes
78	113,8937	-18,7591	17,69 ± 0,08	16,11 ± 0,07	15,41 ± 0,08	T-Tauri candidate	
79	113,8855	-18,7528	17,38 ± 0,05	16,20 ± 0,06	15,41 ± 0,08	T-Tauri candidate	yes
80	113,8847	-18,7625	17,65 ± 0,05	16,35 ± 0,06	15,43 ± 0,08	T-Tauri candidate	yes
81	113,8958	-18,7522	16,99 ± 0,05	15,94 ± 0,06	15,43 ± 0,08	T-Tauri candidate	
82	113,8876	-18,7627	17,65 ± 0,05	16,28 ± 0,06	15,45 ± 0,08	T-Tauri candidate	yes
83	113,8890	-18,7652	16,51 ± 0,05	15,72 ± 0,06	15,46 ± 0,08	field source	
84	113,8925	-18,7674	17,35 ± 0,05	16,13 ± 0,06	15,46 ± 0,08	T-Tauri candidate	
85	113,8959	-18,7666	17,73 ± 0,06	16,19 ± 0,07	15,47 ± 0,08	T-Tauri candidate	
86	113,8924	-18,7585	16,78 ± 0,06	15,75 ± 0,07	15,47 ± 0,08	field source	
87	113,8954	-18,7668	17,05 ± 0,05	15,93 ± 0,06	15,48 ± 0,08	T-Tauri candidate	
88	113,8807	-18,7653	16,58 ± 0,05	15,75 ± 0,06	15,48 ± 0,08	field source	
89	113,8907	-18,7561	17,02 ± 0,05	16,02 ± 0,06	15,52 ± 0,08	T-Tauri candidate	
90	113,8883	-18,7588	17,33 ± 0,05	16,18 ± 0,06	15,53 ± 0,08	T-Tauri candidate	yes
91	113,8911	-18,7688	17,15 ± 0,05	16,02 ± 0,06	15,56 ± 0,08	T-Tauri candidate	
92	113,8827	-18,7694	17,14 ± 0,05	16,01 ± 0,06	15,58 ± 0,08	T-Tauri candidate	
93	113,8905	-18,7601	17,64 ± 0,07	16,56 ± 0,07	15,59 ± 0,08	T-Tauri candidate	yes
94	113,8953	-18,7572	16,97 ± 0,05	15,95 ± 0,06	15,60 ± 0,08	field source	
95	113,8939	-18,7534	17,73 ± 0,05	16,32 ± 0,06	15,61 ± 0,08	T-Tauri candidate	
96	113,8936	-18,7566	17,07 ± 0,05	16,07 ± 0,06	15,63 ± 0,08	T-Tauri candidate	
97	113,8829	-18,7548	17,32 ± 0,05	16,22 ± 0,06	15,65 ± 0,08	T-Tauri candidate	
98	113,8890	-18,7587	17,20 ± 0,06	16,05 ± 0,06	15,65 ± 0,08	T-Tauri candidate	
99	113,9009	-18,7542	16,82 ± 0,05	15,93 ± 0,06	15,65 ± 0,08	field source	
100	113,8872	-18,7634	17,51 ± 0,05	16,29 ± 0,06	15,66 ± 0,08	T-Tauri candidate	
101	113,8916	-18,7554	18,07 ± 0,06	16,63 ± 0,06	15,68 ± 0,08	T-Tauri candidate	yes
102	113,8876	-18,7609	17,64 ± 0,05	16,43 ± 0,06	15,69 ± 0,08	T-Tauri candidate	yes
103	113,8946	-18,7667	17,28 ± 0,05	16,23 ± 0,06	15,69 ± 0,08	T-Tauri candidate	
104	113,9020	-18,7509	17,51 ± 0,05	16,25 ± 0,06	15,70 ± 0,08	T-Tauri candidate	
105	113,8910	-18,7522	17,22 ± 0,05	16,13 ± 0,06	15,71 ± 0,08	T-Tauri candidate	
106	113,8873	-18,7648	17,68 ± 0,05	16,43 ± 0,06	15,73 ± 0,08	T-Tauri candidate	yes
107	113,8936	-18,7581	17,61 ± 0,09	16,23 ± 0,07	15,74 ± 0,08	T-Tauri candidate	
108	113,8923	-18,7558	17,45 ± 0,05	16,32 ± 0,06	15,76 ± 0,08	T-Tauri candidate	
109	113,8916	-18,7644	17,53 ± 0,05	16,34 ± 0,06	15,77 ± 0,08	T-Tauri candidate	
110	113,8885	-18,7677	17,35 ± 0,05	16,26 ± 0,06	15,78 ± 0,08	T-Tauri candidate	
111	113,8914	-18,7698	17,39 ± 0,05	16,30 ± 0,06	15,81 ± 0,08	T-Tauri candidate	
112	113,8951	-18,7702	17,42 ± 0,05	16,44 ± 0,06	15,82 ± 0,08	T-Tauri candidate	yes
113	113,8891	-18,7606	17,60 ± 0,06	16,23 ± 0,07	15,82 ± 0,08	T-Tauri candidate	
114	113,8831	-18,7695	17,41 ± 0,05	16,34 ± 0,06	15,83 ± 0,08	T-Tauri candidate	
115	113,8952	-18,7632	17,85 ± 0,06	16,56 ± 0,06	15,83 ± 0,08	T-Tauri candidate	yes
116	113,8893	-18,7584	16,81 ± 0,05	15,96 ± 0,06	15,83 ± 0,08	field source	
117	113,8915	-18,7562	17,28 ± 0,05	16,25 ± 0,06	15,84 ± 0,08	T-Tauri candidate	
118	113,8919	-18,7601			15,84 ± 0,22		
119	113,8895	-18,7632	17,82 ± 0,05	16,60 ± 0,06	15,88 ± 0,08	T-Tauri candidate	yes
120	113,8937	-18,7609	18,31 ± 0,07	16,85 ± 0,06	15,90 ± 0,08	T-Tauri candidate	yes

Table 4. The J , H and K_S OSIRIS photometry of the sources detected in the direction of SH 2-307 HII region (part 3).

IRS	RA (J2000)	Dec (J2000)	J	H	K	Note	NIR K-band excess?
121	113,8863	-18,7669	17,50 ± 0,05	16,55 ± 0,06	15,99 ± 0,08	T-Tauri candidate	yes
122	113,8862	-18,7643	16,85 ± 0,05	16,29 ± 0,06	16,02 ± 0,08	field source	
123	113,8910	-18,7648	17,64 ± 0,05	16,53 ± 0,06	16,02 ± 0,08	T-Tauri candidate	
124	113,8919	-18,7671	18,09 ± 0,06	16,75 ± 0,06	16,04 ± 0,08	T-Tauri candidate	
125	113,8891	-18,7544	17,64 ± 0,05	16,52 ± 0,06	16,04 ± 0,08	T-Tauri candidate	
126	113,8879	-18,7597	17,69 ± 0,05	16,68 ± 0,07	16,1 ± 0,08	T-Tauri candidate	yes
127	113,8883	-18,7571	17,89 ± 0,06	16,66 ± 0,06	16,13 ± 0,08	T-Tauri candidate	
128	113,8888	-18,7538	17,81 ± 0,05	16,65 ± 0,06	16,14 ± 0,08	T-Tauri candidate	
129	113,8879	-18,7601	17,66 ± 0,06	16,49 ± 0,07	16,14 ± 0,08	field source	
130	113,8867	-18,7621	17,96 ± 0,06	16,79 ± 0,06	16,14 ± 0,08	T-Tauri candidate	yes
131	113,9014	-18,7521	17,95 ± 0,05	16,73 ± 0,06	16,17 ± 0,08	T-Tauri candidate	
132	113,8828	-18,7643	17,73 ± 0,05	16,62 ± 0,06	16,19 ± 0,08	T-Tauri candidate	
133	113,8882	-18,7618	18,05 ± 0,06	16,83 ± 0,07	16,2 ± 0,08	T-Tauri candidate	
134	113,8868	-18,7589	18,21 ± 0,07	16,92 ± 0,08	16,21 ± 0,08	T-Tauri candidate	yes
135	113,8947	-18,7649	18,14 ± 0,06	16,89 ± 0,06	16,22 ± 0,08	T-Tauri candidate	yes
136	113,8864	-18,7513	17,68 ± 0,05	16,63 ± 0,06	16,23 ± 0,08	T-Tauri candidate	
137	113,8939	-18,7667	17,64 ± 0,05	16,67 ± 0,06	16,23 ± 0,08	T-Tauri candidate	
138	113,8840	-18,7703	17,75 ± 0,05	16,67 ± 0,06	16,24 ± 0,08	T-Tauri candidate	
139	113,8945	-18,7526	17,80 ± 0,05	16,68 ± 0,06	16,26 ± 0,08	T-Tauri candidate	
140	113,8945	-18,7605	17,45 ± 0,06	16,53 ± 0,06	16,28 ± 0,08	field source	
141	113,9000	-18,7664	17,85 ± 0,05	16,70 ± 0,06	16,28 ± 0,08	T-Tauri candidate	
142	113,8907	-18,7627	17,97 ± 0,05	16,99 ± 0,06	16,39 ± 0,08	T-Tauri candidate	yes
143	113,8860	-18,7649	18,36 ± 0,06	17,18 ± 0,07	16,40 ± 0,08	T-Tauri candidate	yes
144	113,8817	-18,7627	17,99 ± 0,05	16,87 ± 0,06	16,40 ± 0,08	T-Tauri candidate	
145	113,8808	-18,7579	17,68 ± 0,06	16,75 ± 0,06	16,41 ± 0,08	field source	
146	113,8921	-18,7629	18,41 ± 0,06	17,2 ± 0,07	16,41 ± 0,08	T-Tauri candidate	yes
147	113,8910	-18,7601		17,18 ± 0,08	16,41 ± 0,08		
148	113,8900	-18,7705	17,90 ± 0,05	16,88 ± 0,06	16,41 ± 0,08	T-Tauri candidate	
149	113,8960	-18,7589	18,41 ± 0,06	17,16 ± 0,07	16,42 ± 0,08	T-Tauri candidate	yes
150	113,8920	-18,7689	18,53 ± 0,06	17,06 ± 0,06	16,43 ± 0,08	T-Tauri candidate	
151	113,8804	-18,7533	17,80 ± 0,06	16,93 ± 0,07	16,45 ± 0,08	T-Tauri candidate	yes
152	113,8982	-18,7578	18,27 ± 0,06	17,03 ± 0,06	16,47 ± 0,08	T-Tauri candidate	
153	113,8959	-18,7671	17,58 ± 0,06	16,68 ± 0,06	16,49 ± 0,08	field source	
154	113,8823	-18,7618	18,09 ± 0,06	17,03 ± 0,06	16,51 ± 0,08	T-Tauri candidate	
155	113,8889	-18,7634	18,48 ± 0,06	17,20 ± 0,07	16,54 ± 0,08	T-Tauri candidate	
156	113,8902	-18,7614	18,25 ± 0,07	17,01 ± 0,07	16,54 ± 0,08	T-Tauri candidate	
157	113,8898	-18,7587	18,05 ± 0,06	17,04 ± 0,07	16,56 ± 0,08	T-Tauri candidate	
158	113,8976	-18,7590	18,28 ± 0,06	17,04 ± 0,06	16,57 ± 0,08	T-Tauri candidate	
159	113,8877	-18,7527	18,03 ± 0,05	16,96 ± 0,06	16,58 ± 0,08	field source	
160	113,8948	-18,7658	18,67 ± 0,08	17,35 ± 0,07	16,61 ± 0,08	T-Tauri candidate	yes
161	113,8835	-18,7561	18,33 ± 0,06	17,27 ± 0,07	16,62 ± 0,08	T-Tauri candidate	yes
162	113,9018	-18,7692	18,58 ± 0,07	17,36 ± 0,07	16,62 ± 0,08	T-Tauri candidate	yes
163	113,8873	-18,7524	18,10 ± 0,06	17,09 ± 0,07	16,63 ± 0,08	T-Tauri candidate	
164	113,8827	-18,7706	18,18 ± 0,06	17,13 ± 0,06	16,63 ± 0,08	T-Tauri candidate	
165	113,8867	-18,7650	18,25 ± 0,06	17,07 ± 0,06	16,64 ± 0,08	T-Tauri candidate	
166	113,8824	-18,7649	18,11 ± 0,06	17,09 ± 0,06	16,66 ± 0,08	T-Tauri candidate	
167	113,8959	-18,7664	18,36 ± 0,07	17,20 ± 0,07	16,68 ± 0,08	T-Tauri candidate	
168	113,8983	-18,7638	18,63 ± 0,07	17,43 ± 0,07	16,76 ± 0,08	T-Tauri candidate	yes
169	113,8894	-18,7702	18,86 ± 0,08	17,72 ± 0,07	16,77 ± 0,08	T-Tauri candidate	yes
170	113,8907	-18,7644	17,74 ± 0,05	17,06 ± 0,06	16,78 ± 0,08	field source	
171	113,8860	-18,7622	18,52 ± 0,07	17,35 ± 0,07	16,82 ± 0,08	T-Tauri candidate	
172	113,9023	-18,7579	18,50 ± 0,06	17,39 ± 0,07	16,85 ± 0,08	T-Tauri candidate	
173	113,8917	-18,7686	18,82 ± 0,08	17,64 ± 0,07	16,86 ± 0,08	T-Tauri candidate	yes
174	113,8943	-18,7661	18,63 ± 0,07	17,41 ± 0,07	16,88 ± 0,08	T-Tauri candidate	
175	113,8977	-18,7671	18,78 ± 0,07	17,60 ± 0,07	16,88 ± 0,08	T-Tauri candidate	yes
176	113,8867	-18,7549	18,96 ± 0,08	17,64 ± 0,07	16,98 ± 0,08	T-Tauri candidate	
177	113,8882	-18,7623	18,50 ± 0,07	17,57 ± 0,08	16,98 ± 0,08	T-Tauri candidate	yes
178	113,8976	-18,7640	18,64 ± 0,07	17,46 ± 0,07	16,98 ± 0,08	T-Tauri candidate	
179	113,8863	-18,7570	18,72 ± 0,07	17,70 ± 0,07	17,00 ± 0,08	T-Tauri candidate	yes